PCCP

Accepted Manuscript

ROYAL SOCIETY OF CHEMISTRY

www.rsc.org/pccp

ARTICLE TYPE www. rsc.org/xxxxxx | XXXXXXXX

Two-Dimensional Tricycle Arsenene with a Direct Band Gap

ShuangYing Ma[a], Pan Zhou[b], L. Z. Sun[b†] and K. W. Zhang[a ‡]

Received Xth XXXXXXXXXX 20XX, Accepted Xth XXXXXXXXX 20XX
First published on the web Xth XXXXXXXXXX 200X
DOI: 10.1039/b000000x

Based on a comprehensive investigation including ab initio phonon and finite-temperature molecular dynamics calculations, we find that two-dimensional tricycle-shaped arsenene (T-As) is robust and even stable under high temperature. T-As is energetically comparable to previously reported chair-shaped arsenene (C-As) and more stable than stirrup-shaped arsenene (S-As). In contrast to C-As and S-As, the monolayer T-As is a direct band gap semiconductor with an energy gap of 1.377 eV. Our results indicate that the electronic structure of T-As can be effectively modulated by stacking, strain, and patterning, which shows great potential of T-As in future nano-electronics. Moreover, by absorbing H or F atoms on the surface of T-As along a specific direction, nanoribbons with desired edge type even width can be obtained, which is suitable for fabrication of nano-devices.

1 Introduction

Synthesis of graphene and subsequent extensive researches have established the foundation for further studying other two-dimensional (2D) atomic layer materials[1–4]. Currently, considerable endeavor has been devoted to discover 2D monolayer materials other than graphene, such as hexagonal BN[1,5], transition-metal dichalcogenides (TMDs)[1,6], as well as group IV[7–10], II-VI[11–13], and III-V compounds[14–16] metastable monolayer materials. Recently, monolayer puckered black-phosphorene[17] composed purely of phosphorus element shows great potential for fabricating unique nanoelectronic and optoelectronic devices in post-silicon epoch due to its peculiar properties, such as high carrier mobility[18,19], highly anisotropic transport[17], negative Poisson's ratio[20], excellent optical and thermoelectric responses[21]. Stimulated by these works, another ten layered phosphorene phases[22–25] are also predicted to be stable, which expands possible application prospect of 2D phosphorus sheets. These achievements prompt people to speculate that whether the arsenic and antimony elements can also form 2D nanosheets stably due to their very similar electron configuration to that of phosphorus element. Amazingly, that is what happens. The stirrup- and chair-shaped monolayer configurations of arsenic (arsenene)[26–30] and antimony (antimonene)[26,31] elements are also predicted to be stable. Similar to the case of layered black-phosphorene, arsenene and antimonene also possess unique properties, such as high carrier mobility[32], controllable topological phase transition[33–35], ultra-high mechanical stretchability[34] and negative Poisson's ratios[36]. In contrast to the high carrier mobility found for 2D arsenene[32], cutting 2D arsenene and antimonene into nanoribbons would cause small carrier mobilities[37]. Recent studies on the group-V-group-IV hetero-bilayer structures[38,39], such as arsenene-graphene system, showed controllable Schottky barrier. The work of Hsu et al.[40] reported that planar bismuth and antimony honeycombs can be potential new 2D topological insulator platforms for room-temperature applications. The above mentioned unique properties of layered arsenene and antimonene suggest their promising applications in nano-electronics.

In order to expand the application prospect of 2D arsenene, it is necessary to discover its allotropes as many as possible. Our previous work indicated that red color tricycle-shaped phosphorene(T-P)[25] shows dynamically and remarkably thermodynamical stability comparable to that of black one. Considering the chemical similarity between phosphorus and arsenic elements, we propose that tricycle-shaped arsenene should also be dynamically stable.

In this article, we performed first-principles method to study the stability of tricycle-shaped arsenene, named T-As for short. The calculations indicate that T-As is energetically more stable than stirrup-shaped arsenene (S-As)[27]. Moreover, in contrast to the previously reported two kinds of arsenene[26,27], the monolayer T-As is a direct band gap semiconductor with a gap of 1.377 eV. The value and type of its band gap can be effectively modulated by in-layer uniaxial strain, patterning, and multi-layer stacking. Moreover, adsorption of foreign atoms such as H and F can be efficient scissor to cut T-As with specific edge configuration, such as zigzag and armchair ones.

2 Computational Details

We performed first-principles density functional theory as implemented in the VASP code[41,42] to investigate the equilib-

[a] *School of Physics and Optoelectronics, Xiangtan University, Xiangtan 411105, China. E-mail: kwzhang@xtu.edu.cn*
[b] *Hunan Provincial Key laboratory of Thin Film Materials and Devices, School of Material Sciences and Engineering, Xiangtan University, Xiangtan 411105, China. E-mail: lzsun@xtu.edu.cn*

rium structures, stabilities, and electronic properties of T-As. The electron-electron interaction was treated with a generalized gradient approximation (GGA) proposed by Perdew, Burke, and Ernzerhof (PBE)[43]. The projector-augmented wave (PAW)[44,45] method was used to describe the interaction between valence electrons and core. A kinetic-energy cutoff of 550 eV was selected for the plane wave basis set and a vacuum space of 15 Å was set to avoid the interaction between neighboring images. The Brillouin zone was sampled using 13×13×1 Monkhorst-Pack k-pint scheme. All systems were fully relaxed until the total energy converges to 10^{-6} eV and non of the residual Hellmann-Feynman forces on the ions exceed 0.01 eV/Å. The relative energetic stability of three arsenenes can be evaluated by comparing their cohesive energy per atom. To verify the dynamic and themodynamic stability of T-As, the phonon spectrum calculations and ab initio molecular dynamics (AIMD) simulation were also performed, respectively.

3 Results and Discussions

The optimized structural configuration of T-As is shown in Fig. 1, which is very similar to that of T-P which can be viewed as a combination of the segments of the chair- and stirrup-shaped arsenene (C-As and S-As for short respectively). Thereby, T-As, like T-P, also has a rectangular lattice with Pbcm (No. 57) space group symmetry. As is displayed in Fig. 1, although the unit cell of T-As contains 8 As atoms, there are only two kinds of nonequivalent atoms labeled as A and B, respectively. The A and B atoms are exactly originated from the fragment of S- and C-As, respectively. As is depicted in Fig. 1, the two kinds of nonequivalent As atoms lead to three types of nonequivalent bond lengths (l_1, l_2, and l_3) and angles (∠1, ∠2 and ∠3). The value of l_1, l_2, and l_3 is 2.507, 2.501, and 2.513 Å, respectively; the value of ∠1, ∠2, and ∠3 is 93.309, 101.109, and 90.482 °, respectively. Meanwhile, the thickness of monolayer T-As is 4.335 Åas listed in Tab. 1 , which is 0.635 Å thicker than that of T-P phase. This phenomenon can be ascribed to the weaker electronegativity of As atom than that of P atom, which results in much longer bond length (≈2.5 Å) of As-As than that of P-P (≈2.2 Å). Meanwhile, the thickness of T-As is much larger than that of C-As (1.398 Å) and S-As (0.680 Å). Wang et al.[30] reported that the structure of stirrup-shaped arsenene would be dependent on the functional, namely the configuration optimized by PBE functional[43] is different from those obtained by PBEsol, LDA and D3+BJ[46,47]. Considering the reliability of the results, we have further optimized the structure of T-As with PBEsol, LDA and D3+BJ functional, respectively, and a detailed analysis indicates that the configuration of T-As is not dependent on the functional. Therefore, we adopt the results

Table 1 Lattice constants (a and b), bond length (l_1, l_2 and l_3), bond angle (angle 1, angle 2 and angle 3), thickness (d), and space group (SG) of T-As monolayer.

	a(Å)	*b*(Å)	l_1(Å)	l_2(Å)	l_3(Å)	∠1(°)	∠2(°)	∠3(°)	d(Å)	SG
T-As	3.647	9.582	2.507	2.501	2.513	93.309	101.109	90.482	4.335	Pbcm

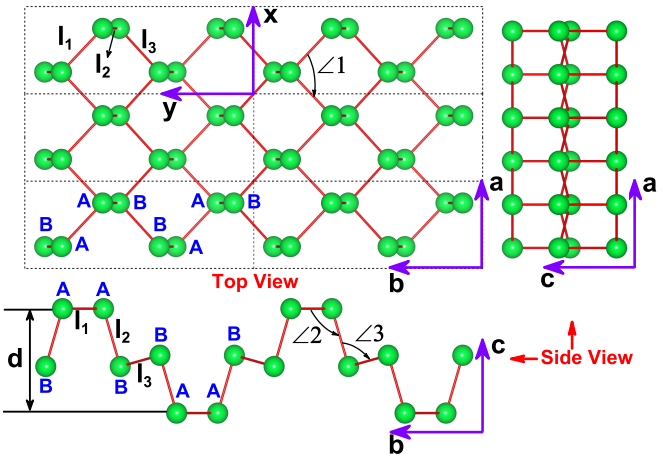

Fig. 1 Top and side view of 3×2×1 supercell of optimized structure of T-As. The balls in green represent arsenic atoms. d is the thickness of the quasi-2D T-As. The letter A and B stands for two nonequivalent As atoms in a unit cell of T-As. The l_1, l_2 and l_3 stand for nonequivalent bond length of T-As, as well as nonequivalent bond angle angle 1, angle 2 and angle 3.

obtained by PBE functional in the following discussion. It is worthy to mention that the flat configuration of T-As is still remained under the strain, in contrast to the case of S-As[30].

Our calculations indicate that the total energy per atom of T-As is 21 meV lower than that of S-As and 16 meV higher than that of C-As, which indicates that T-As is energetically more stable than S-As. Thereby, to some extent, T-As is more easily to be observed than S-As in experiment. The dynamical stability of T-As is confirmed by phonon spectrum and corresponding density of states[48]. As is displayed in Fig. 2, none of soft phonon modes can be found for T-As indicating its dynamical stability. Meanwhile, ab initio molecular dynamics (AIMD) simulation as implemented in CP2K/QUICKSTEP program package (http://www.cp2k.org)[49] was also performed to further confirm its thermodynamics stability. The CP2K package employs a mixed Gaussian and plane-wave basis set and norm-conserving pseudopotentials. The Kohn-Sham orbitals were expanded in the basis of Gaussian functions by employing double zeta valence polarized basis sets which are optimized for the GTH pseudopotentials (DZVP-MOLOPT-SR-GTH)[50]. A 400 Ry cut-off energy was used for plane-wave basis set. In the AIMD simulations the NVT ensemble was used with a target temperature of 600 K, maintained with

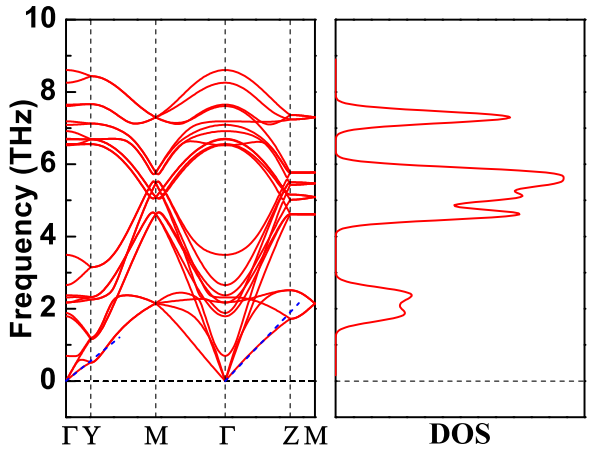

Fig. 2 Phonon band structures and density of states of monolayer T-As.

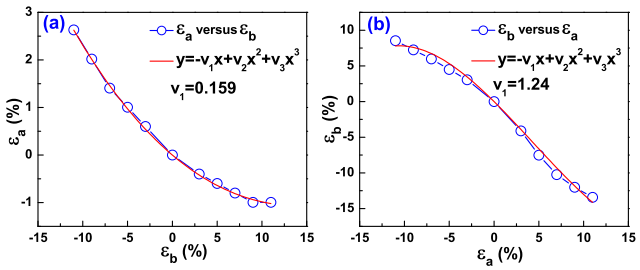

Fig. 3 (a)ε_a versus ε_b. (b) ε_b versus ε_a. The blue circles are calculated data which is fitted by function of y=-v_1x+v_2x^2+v_3x^3 denoted by red line, with v_1 as the linear Poisson's ratio.

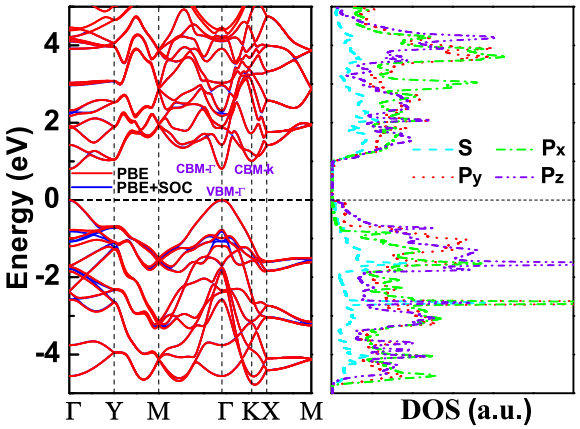

Fig. 4 Band structure and the partial density of states (PDOS) of T-As.

a Nosé-Hoover chain thermostat state. The time step was set as 1 fs and a 5x3x1 supercell was adopted in the simulations. In the whole simulation period, the structure of T-As can be maintained, which indicates that T-As is thermodynamically stable.

Firstly, we focus on the mechanical properties of T-As. The slope of the longitudinal acoustic branch near Γ point, which reflects the sound velocity and in-plane stiffness, is shown in Fig. 2. The speed of sound along the Γ-Y direction of T-As ($v_s^{\Gamma-Y}$=10.72 km/s) is 3.16 km/s smaller than that along Γ-X orientation ($v_s^{\Gamma-Y}$=13.88 km/s). The result indicates that the stiffness of T-As is anisotropic that the value along $\vec{a}$ direction is larger than that along $\vec{b}$ orientation. When deformation is applied along $\vec{b}$ direction, the induced strain in the $\vec{a}$ direction is shown in Fig. 3 (a). The calculated data (blue circular) behaves as a strongly nonlinear feature, which can be well fitted by function of y=-v_1x+v_2x^2+v_3x^3. The linear parameter v_1 is 0.159 and can be taken as the linear Poisson's ratio. Similarly, the linear Poisson's ratio in the $\vec{a}$ direction is shown in Fig. 3 (b). The corresponding linear Poisson's ratio is 1.24 which is nearly eight times larger than that in $\vec{b}$ orientation, reflecting the larger rigidity of T-As along $\vec{b}$ orientation than that along $\vec{a}$ direction. This result is well agreement with the conclusion obtained from the speed of sound of T-As above.

The previously reported C-As and S-As are all indirect semiconductors, but for T-As, our DFT-PBE calculations indicate that the monolayer T-As is a direct band gap semiconductor with the energy gap of 0.818 eV, as shown in Fig. 4. Due to the fact that PBE functional always underestimates the band gap of semiconducting materials, we adopted HSE06

functional[51,52] to further study its band gap. The corrected energy-gap value is 1.377 eV. We should try to understand the reason why C-As and S-As possess different band type from T-As. We further calculate the crystal orbital Hamiltonian population (COHP) of C- and S-As, as shown in Fig. S1 (a) and (e), respectively. The A1 state of C-As is contributed by bonding state, while its B1 and C1 orbitals are all ascribed to anti-bonding states. The partial charge density (PCD) of B1 and C1 are shown respectively in Fig. S1 (b) and (c), where the orbital of B1 is more localized than that of C1, resulting in higher energy of B1 than that of C1. Therefore, the C1 state rather than B1 state becomes the conduction band minimum (CBM) of C-As, leading to different k point for A1 and C1 point, which is the reason of C-As shows as an indirect semiconductor. For S-As, as shown in Fig. S1 (e), its A2 and C2 state are all contributed by anti-bonding states. A detailed analysis shows that the anti-bonding feature of A2 is weaker than that of C2, which can be explained by the PCD of A2 and C2 orbitals, as shown in Fig. S1 (g) and (h), respectively. Obviously, there is charge overlapping for C2 state, which results in higher energy of A2 state than that of C2 state. Therefore, A2 point rather than C2 point becomes the VBM of S-As, which leads to different k point for VBM and CBM of S-As producing indirect band gap of S-As. But for T-As, there are not any other states competing with its VBM or CBM, therefore, its VBM and CBM all locate at Γ point as shown in Fig. 4 behaving as direct band gap semiconductor. Its VBM is primarily contributed by p_y+p_z orbitals of As atoms; while the CBM is determined by s+p orbitals. Around VBM, the s and p orbitals show similar electronic resonance, indicating strong hybridization between As atoms. We further consider the effect of the spin-orbit coupling on band structure of T-As. The result shows that the spin-orbit coupling effect can be neglected for T-As.

On the basis of the monolayer T-As, we propose its possible stacking configurations. The optimized geometries with AA and AB stacking order are shown in Fig. S2. The interlayer distance is 1.754 and 3.638 Å for bilayer T-As with AA and AB stacking, respectively. Obviously, the interlayer distance of AA stacking is much smaller than that of AB stacking due to its one layer convex confronting to its neighboring layer concave like a nested hat. The band structures as shown in Fig. 4 and 5 indicate that multilayer T-As with AA stacking will change from direct semiconductor (N=1, Fig. 4) to indirect ones (2≤N<8, Fig. 5 (a)-(b)) accompanied decreasing in the energy gap, and then further changes to a metal with the increasing in N. Through detailed analysis, we find that the phenomena can be ascribed to the competition of the states of VBM-Γ, CBM-Γ and CBM-K, as shown in Fig. 5 (a)-(c). The energy level of VBM-Γ increases with the increase in N. Meanwhile, the energy levels of CBM-K and CBM-Γ drop with respect to the Fermi level. It should be noted that the de-

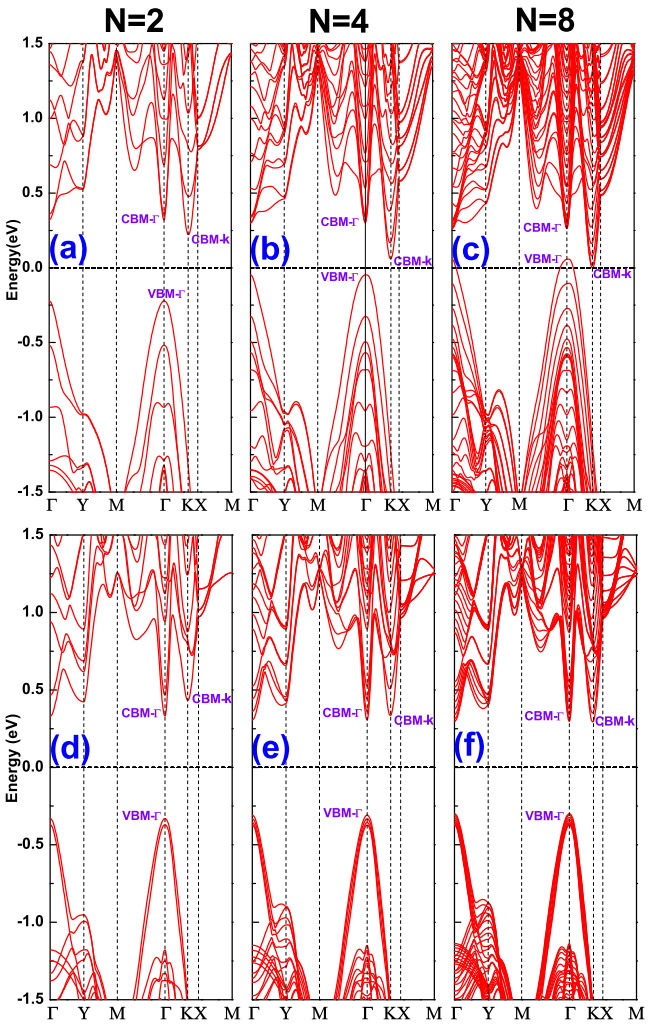

Fig. 5 (a), (b) and (c) show the band structures of multilayer T-As with AA stacking. (d), (e) and (f) show the band structures of multilayer T-As with AB stacking. N stands for the number of layer. The VBM-Γ, CBM-Γ, and CBM-K stands for valence and conduction bands located at Γ and *K* points, respectively.

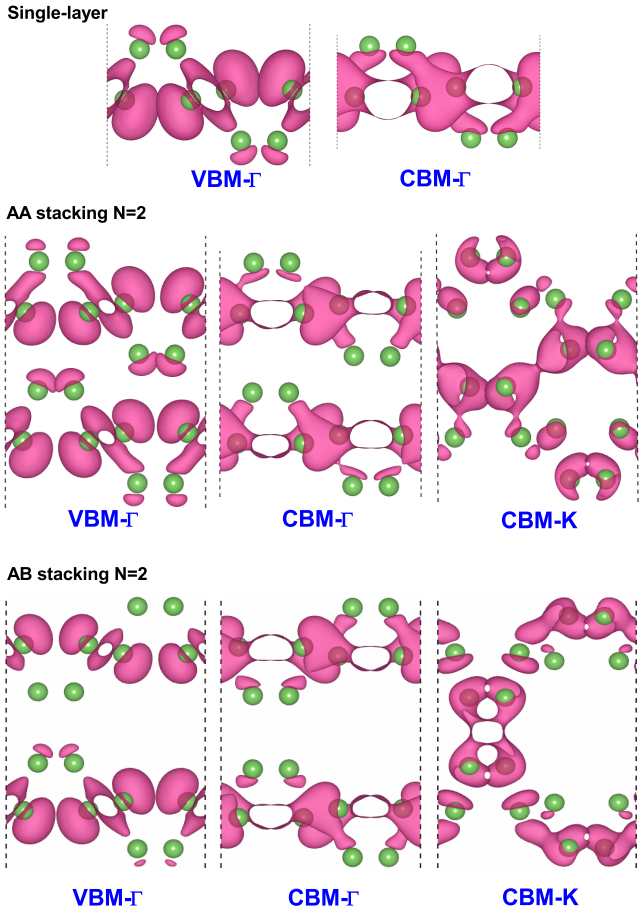

Fig. 6 Partial charge density of monolayer and bilayer (AA and AB stacking) T-As with isosurface of 0.0015e/Å^3. The VBM-Γ, CBM-Γ, and CBM-*K* stands for partial charge density of valence and conduction bands located at Γ and *K* points, respectively. The labels VBM-Γ, CBM-Γ, and CBM-*K* are the same as shown in Fig. 5.

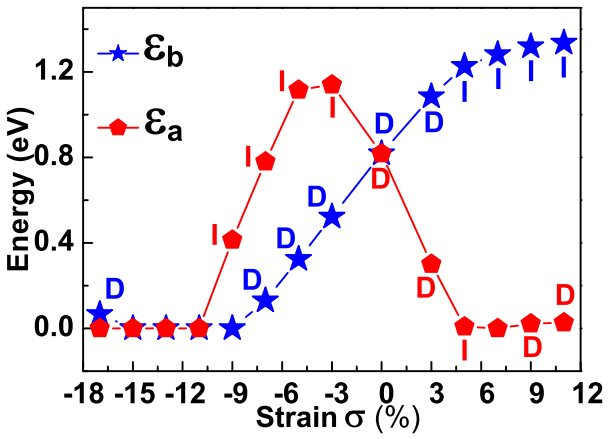

Fig. 7 Dependence of the electronic structure of T-As on the uniaxial stress. The letter D, I and M is respectively stands for direct bandgap, indirect bandgap and metal.

crease amplitude of CBM-K is much larger than that of CBM-Γ resulting in the direct-indirect transition of its band structure. Moreover, the fast-rising of the energy level of VBM-Γ leads to the transition from indirect semiconductor to a metal. As is depicted in Fig. 6, the PCDs of the monolayer T-As at VBM-Γ and CBM-Γ points are very similar to those of its bilayered AA and AB stacking at corresponding points, which suggests that the VBM-Γ and CBM-Γ states are mainly contributed by interaction between the same layer rather than the interlayer As atoms. While for CBM-K states of bilayered T-As, their PCDs show obvious charge overlap between adjacent layers, which indicates that wavefunction overlap rather than van der Waals effect plays the leading role in the interlayer interaction. Moreover, clearly, the evolution of CBM-K states are dominated by the charge overlap. Take bilayered AA stacking for example, its CBM-Γ state is little affected by increasing layer since it is mainly ascribed to interaction between in-plane As atoms, so with N increasing to two from one, the energy of the CBM-Γ state only has little decrease due to size effect, but the CBM-K state has a much energy reduction due to the remarkable charge overlap. Therefore, the CBM of T-As changes from the CBM-Γ to CBM-K point, which results in a direct-indirect transition, as shown in Fig. 5 (a). Meanwhile, the energy of the VBM-Γ state increases continuously with increasing of N due to size effect. In the end, the cooperation between CBM-K and VBM-Γ leads to the transition from indirect semiconductor to metal. Similar case is also found for T-As with AB stacking. However, due to the much larger interlayer distance as shown in Fig. S2, the interlayer wavefunction overlap in multilayer T-As with

AB stacking is smaller than that in AA stacking. Therefore, although the tendency of transition of energy band structures of T-As with AB stacking is similar to that of T-As with AA stacking, the transition speed of the energy structure of T-As with AB stacking is slower than that of T-As with AA stacking, as shown in Fig. 5 (d)-(f). We can not observe the direct-indirect transition until the N>8 for T-As with AB stacking. The dependence of the band gap on the thickness produces the T-As show wide range adjustability of its electronic property.

Another intriguing issue of T-As is the sensitive dependence of its band gap on in-plane strain exerted along two axial directions, as shown in Fig. 7. T-As is a direct-band-gap semiconductor under zero strain. When applied stretching stain along axial vector $\vec{a}$, the energy gap of T-As tends to decrease sharply and then increase slightly with the increase in strain. T-As firstly transforms into an indirect semiconductor at σ=5% and then changes into a metal at σ=7%, after that, with strain further increasing to σ=9%, it again turns back a direct semiconductor with a energy gap of 0.022 eV. Except for at σ=7%, the energy band type of T-As remains direct feature and their VBM and CBM all locate at or very near to Γ point, as shown in Fig. S3 (a). When apply compressive strain along axial vector $\vec{a}$ and it lies in the range of -3%≤σ≤-9%. The T-As changes into an indirect semiconductor. The value of its band gap firstly increases to 1.14 eV at σ=-3%, and then decreases to zero at σ=-11%. In the process, as shown in Fig. S3 (a), its VBM always locates at Γ point, but the location of its CBM changes from Γ point to the point between Γ and X. As shown in Fig. 7, when apply tensile strain along axial vector $\vec{b}$, the T-As turns to an indirect semiconductor when σ≥5%. In the process, its VBM always locates at Γ point, whereas its CBM shifts from Γ point to the point between Γ and X. Its energy gap can be enlarged from 0.818 (σ=0%) to 1.336 eV (σ=11%). When applied compressive strain along axial $\vec{b}$, however, the situation is reversal. The energy gap of T-As reduces sharply and finally changes to zero at σ=-9%, and then again turns into direct semiconductor with an energy gap of 0.066 eV at σ=-17%. In the compression process, before T-As becoming a metal at σ=-9%, its VBM and CBM all locates at Γ point, similar to the case of unstrained T-As. But, at the compression strain of σ=-17%, the locations of its VBM and CBM all locate in the points between Γ and X. The above results indicate that external uniaxial strain can effectively tune the band gap and type of T-As. Such feature of T-As is significant for its application in nanoelectronics.

An effective approach to modulate the electronic properties of the 2D system and promote its applications is patterned it into one dimensional (1D) nanoribbons, such as graphene nanoribbon (GNR). It is of both fundamental interest and technological importance to study the electronic properties of nanoribbons originated from 2D T-As. Considering the zigzag and armchair conventional notation of GNR, we take the zigzag

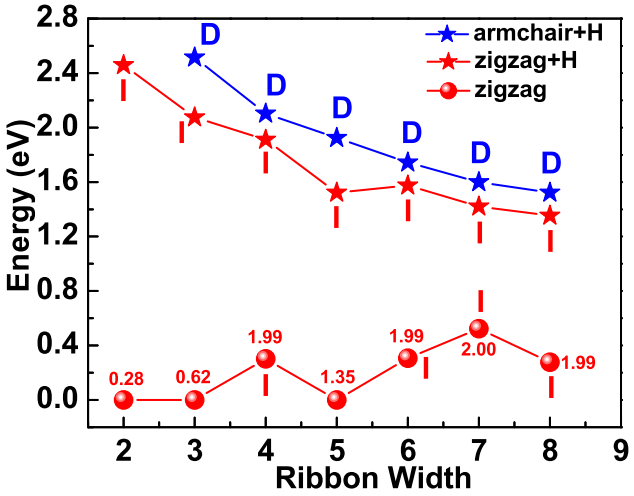

Fig. 8 Band gap of T-As nanoribbon in function of ribbon width (N). The letter I and D stand for indirect and direct semiconductor, respectively. The number stands for corresponding magnetic moment with unit of μ_B.

and armchair edge T-As nanoribbon (Z-T-AsNR and A-T-AsNR) as examples to study their electronic properties, the structures of T-AsNR are shown in Fig. S4. Firstly, we study the properties of Z-T-AsNRs and A-T-AsNRs with their edges passivated by H atoms. As is shown in Fig. 8, the H-passivated Z-T-AsNRs and A-T-AsNRs are indirect and direct semiconductors, respectively. With increasing of the width of nanoribbons, the energy gap of them tend to decrease. While for the edge-bared T-AsNRs, we find that only the Z-T-AsNRs can be available and the A-AsNRs is unstable. The calculations indicate that the edge-bared Z-T-AsNRs behave as ferromagnetic metals or semiconductors according to their different ribbon width. The results show that Z-T-AsNRs are potential candidate for spintronic devices. Interestingly, we find that the adsorption of H or F atoms on the surface of T-As behaves as effective scissors to pattern the 2D T-As into 1D nanoribbons with desired edge type. The results indicate that when absorbing one H or F atom on a As atom, As will lose bonding with its one NN As and re-bonds with its another two neighbor As atoms. Therefore, we predict that in experiments 1D T-As nanoribbons can be obtain through H or F atoms injection along specific direction, which is suitable for the fabrication of nanodevices in experiments.

4 Conclusions

A 2D tricycle-shaped arsenene (T-As) is predicted to be robust and can remain its original configuration even at 600 K, based on a comprehensive investigation including ab initio phonon and finite-temperature molecular dynamics calculations. T-As is energetically comparable to previously reported chair-shaped arsenene (C-As) and much stable than stirrup-shaped arsenene (S-As). In contrast to C-As and S-As, the monolayer T-As is a direct band gap semiconductor with a energy gap of 1.377 eV, which is suitable for 2D naxno-electronics applications. Multi-layer T-As undergoes direct-indirect transition and further transforms into metal ascribed to the wave function overlap between the layers. Such band type modulation can also occur by applying uniaxial stress. The electronic structure of T-As sensitively depends on uniaxial stress. By absorbing H or F atoms on T-As surface along a specific direction, nanoribbons with desired edge type even width can be obtained and demonstrate remarkable size effect. Our results indicate great potential of T-As in future nano-electronics.

Acknowledgement

This work was financially supported by the National Natural Science Foundation of China (Grant Nos. 11574260 and 11274262) and the Natural Science Foundation of Hunan Province, China (Grand No. 14JJ2064).

References

1 K. Novoselov, D. Jiang, F. Schedin, T. Booth, V. Khotkevich, S. Morozov and A. Geim, *Proc. Natl. Acad. Sci. U.S.A*, 2005, **102**, 10451–10453.
2 K. Novoselov, A. K. Geim, S. Morozov, D. Jiang, M. Katsnelson, I. Grigorieva, S. Dubonos and A. Firsov, *Nature*, 2005, **438**, 197–200.
3 A. K. Geim and K. S. Novoselov, *Nat. Mater.*, 2007, **6**, 183–191.
4 A. C. Neto, F. Guinea, N. Peres, K. S. Novoselov and A. K. Geim, *Rev. Mod. Phys.*, 2009, **81**, 109.
5 C. Jin, F. Lin, K. Suenaga and S. Iijima, *Phys. Rev. Lett.*, 2009, **102**, 195505.
6 P. Joensen, R. Frindt and S. R. Morrison, *Mater. Res. Bull.*, 1986, **21**, 457–461.
7 S. Cahangirov, M. Topsakal, E. Aktürk, H. Şahin and S. Ciraci, *Phys. Rev. Lett.*, 2009, **102**, 236804.
8 P. De Padova, C. Quaresima, C. Ottaviani, P. M. Sheverdyaeva, P. Moras, C. Carbone, D. Topwal, B. Olivieri, A. Kara, H. Oughaddou *et al.*, *Appl. Phys. Lett.*, 2010, **96**, 261905.
9 B. Feng, Z. Ding, S. Meng, Y. Yao, X. He, P. Cheng, L. Chen and K. Wu, *Nano Lett.*, 2012, **12**, 3507–3511.
10 Y. Miyamoto and B. D. Yu, *Appl. Phys. Lett.*, 2002, **80**, 586–588.
11 A. R. Botello-Méndez, F. López-Urías, M. Terrones and H. Terrones, *Nano Lett.*, 2008, **8**, 1562–1565.
12 M. Topsakal, S. Cahangirov, E. Bekaroglu and S. Ciraci, *Phys. Rev. B*, 2009, **80**, 235119.
13 W. Wu, P. Lu, Z. Zhang and W. Guo, *ACS Appl. Mater. Interfaces*, 2011, **3**, 4787–4795.
14 A. Du, Z. Zhu, Y. Chen, G. Lu and S. C. Smith, *Chem. Phys. Lett.*, 2009, **469**, 183–185.
15 H. Şahin, S. Cahangirov, M. Topsakal, E. Bekaroglu, E. Akturk, R. T. Senger and S. Ciraci, *Phys. Rev. B*, 2009, **80**, 155453.
16 H. Li, J. Dai, J. Li, S. Zhang, J. Zhou, L. Zhang, W. Chu, D. Chen, H. Zhao, J. Yang *et al.*, *J. Phys. Chem. C*, 2010, **114**, 11390–11394.
17 H. Liu, A. T. Neal, Z. Zhu, Z. Luo, X. Xu, D. Tománek and P. D. Ye, *ACS nano*, 2014, **8**, 4033–4041.
18 L. Li, Y. Yu, G. J. Ye, Q. Ge, X. Ou, H. Wu, D. Feng, X. H. Chen and Y. Zhang, *Nat. Nanotech.*, 2014, **9**, 372–377.
19 J. Qiao, X. Kong, Z.-X. Hu, F. Yang and W. Ji, *Nat. Commun.*, 2014, **5**, 4475.
20 J.-W. Jiang and H. S. Park, *Nat. commun.*, 2014, **5**, 4727.
21 R. Fei, A. Faghaninia, R. Soklaski, J.-A. Yan, C. Lo and L. Yang, *Nano Lett.*, 2014, **14**, 6393–6399.
22 J. Guan, Z. Zhu and D. Tománek, *Phys. Rev. Lett.*, 2014, **113**, 046804.
23 Z. Zhu and D. Tománek, *Phys. Rev. Lett.*, 2014, **112**, 176802.
24 M. Wu, H. Fu, L. Zhou, K. Yao and X. C. Zeng, *Nano Lett.*, 2015, **15**, 3557–3562.
25 T. Zhao, C. He, S. Ma, K. Zhang, X. Peng, G. Xie and J. Zhong, *J. Phys.: Condens. Matter.*, 2015, **27**, 265301.
26 S. Zhang, Z. Yan, Y. Li, Z. Chen and H. Zeng, *Angew. Chem. Int. Ed.*, 2015, **127**, 3155–3158.
27 C. Kamal and M. Ezawa, *Phys. Rev. B*, 2015, **91**, 085423.
28 P. Chun-Ying, Y. Xiao-Tao, J. Hua-Long, Z. Fei-Wu, L. Zhi-Wen, H. Jun-Bao and Z. Da-Wei, *Chinese Phys. B*, 2015, **24**, 036301.
29 L. Kou, Y. Ma, X. Tan, T. Frauenheim, A. Du and S. Smith, *J. Phys. Chem. C*, 2015, **119**, 6918–6922.
30 Y. Wang and Y. Ding, *J. Phys.: Condens. Matter.*, 2015, **27**, 225304.
31 G. Wang, R. Pandey and S. P. Karna, *ACS Appl. Mater. Inter.*, 2015.
32 Z. Zhang, J. Xie, D. Yang, Y. Wang, M. Si and D. Xue, *Appl. Phys. Express*, 2015, **8**, 055201.
33 H. Zhang, Y. Ma and Z. Chen, *Nanoscale*, 2015, **7**, 19152–19159.
34 M. Yang and W.-M. Liu, *arXiv preprint arXiv:1501.04350*, 2015.
35 M. Zhao, X. Zhang and L. Li, *Sci. Rep.*, 2015, **5**, 16108.
36 J. Han, J. Xie, Z. Zhang, D. Yang, M. Si and D. Xue, *Appl. Phys. Express*, 2015, **8**, 041801.
37 Y. Wang and Y. Ding, *Nanoscale Res. Lett.*, 2015, **10**, 1–10.
38 Y. Wang and Y. Ding, *Phys. Chem. Chem. Phys.*, 2015, **17**, 27769–27776.
39 C. Xia, B. Xue, T. Wang, Y. Peng and Y. Jia, *Appl. Phys. Lett.*, 2015, **107**, 193107.
40 C.-H. Hsu, Z.-Q. Huang, F.-C. Chuang, C.-C. Kuo, Y.-T. Liu, H. Lin and A. Bansil, *New. J. Phys.*, 2015, **17**, 025005.
41 G. Kresse and J. Furthmüller, *Phys. Rev. B*, 1996, **54**, 11169.
42 G. Kresse and J. Furthmüller, *Comput. Mater. Sci.*, 1996, **6**, 15–50.
43 J. P. Perdew, K. Burke and M. Ernzerhof, *Phys. Rev. Lett.*, 1996, **77**, 3865.
44 P. E. Blöchl, *Phys. Rev. B*, 1994, **50**, 17953.
45 G. Kresse and D. Joubert, *Phys. Rev. B*, 1999, **59**, 1758.
46 S. Grimme, J. Antony, S. Ehrlich and H. Krieg, *J. Chem. Phys.*, 2010, **132**, 154104.
47 S. Grimme, S. Ehrlich and L. Goerigk, *J. Comput. Chem.*, 2011, **32**, 1456–1465.
48 K. Parlinski, Z. Li and Y. Kawazoe, *Phys. Rev. Lett.*, 1997, **78**, 4063.
49 J. VandeVondele, M. Krack, F. Mohamed, M. Parrinello, T. Chassaing and J. Hutter, *Comput. Phys. Commun.*, 2005, **167**, 103–128.
50 J. VandeVondele and J. Hutter, *J. Chem. Phys.*, 2007, **127**, 114105.
51 J. Paier, M. Marsman, K. Hummer, G. Kresse, I. C. Gerber and J. G. Ángyán, *J. Chem. Phys.*, 2006, **124**, 154709.
52 J. Paier, M. Marsman, K. Hummer, G. Kresse, I. Gerber and J. Ángyán, *J. Chem. Phys.*, 2006, **125**, 9901.